# Fabrication of $TiO_2/C_3N_4$ heterostructure for enhanced photocatalytic Z-scheme overall water splitting

Junqing Yan[a], Huan Wu[a], Hong Chen[a], Yunxia Zhang[a], Fuxiang Zhang[b], Shengzhong Frank Liu[a,b,*]

[a] Shaanxi Engineering Lab for Advanced Energy Technology, School of Materials Science and Engineering, Shaanxi Normal University, Xi'an, 710119, PR China
[b] State key Laboratory of Catalysis, iChEM, Dalian Institute of Chemical Physics, Dalian National Laboratory for Clean Energy, Chinese Academy of Sciences, Dalian, 116023, PR China

## ABSTRACT

Z-scheme overall water splitting based on semiconductors has been extensively investigated for hydrogen fuel production from renewable resources. The Z-scheme involves two different kinds of semiconductor photocatalysts and the closely related oxidation-reduction processes. However, the two separated photocatalytic processes require good production and separation of carriers, which greatly limit the efficiency of overall water splitting. Herein, to solve the recombination problem of photogenerated charge carriers, we developed a one-step hydrothermal process to synthesize $TiO_2/C_3N_4$ heterojunctions. The layered g-$C_3N_4$ provides the template and guidance for the anatase $TiO_2$ heterogeneous nucleation with (001) facet exposed. Meanwhile, the bulk g-$C_3N_4$ turned into thicker nanosheets through the self-exfoliation with the growth of $TiO_2$. The heterojunctions with $TiO_2$ (001) facet exposed ensure the efficient separation of photogenerated carriers, which accordingly enhances the photocatalytic hydrogen evolution. $WO_3$ and $BiVO_4$ are chosen as photocatalysts for the half reaction of oxygen evolution. With suitable redox mediators i.e. $I^-/IO_3^-$ or $Fe^{2+}/Fe^{3+}$, the overall water splitting to $H_2$ and $O_2$ could be achieved. If $\beta$-$Ni(OH)_2$, was loaded on the oxygen evolution photocatalysts, the efficiency of Z-scheme water splitting was greatly enhanced. Under the monochromatic light irradiation of LEDs, the apparent quantum efficiency (AQE) values for the Z-scheme of $TiO_2/C_3N_4$, $\beta$-$Ni(OH)_2$/$WO_3$(PtOx) and $I^-/IO_3^-$ system were 4.94% and 4.01% under 365 and 405 nm, respectively. The heterojunction strategy for enhancing Z-scheme overall water splitting may give us some hints on the design of composite systems for overall water splitting.

© 2016 Elsevier B.V. All rights reserved.

## 1. Introduction

The solar energy is an unexhausted and clean resource, which is expected to replace the traditional fossil energy in the future. Among the applications of solar energy, solar-induced water splitting into $H_2$ and $O_2$ using semiconductors has been enormously studied [1–6]. However, the photocatalytic overall water splitting is extremely challenging due to the fact that it is not only an uphill reaction required to thermodynamically overcome the Gibbs free energy of 237 KJ/mol, but also involves an four-electrons/holes process with the relatively complicated and difficult multi-steps [7–10]. To receive a satisfying water overall splitting efficiency, the semiconductor/photocatalyst should not only possess suitable conduction band (for hydrogen generation) and valance band (for oxygen generation) positions, but also the high separation efficiency of photogenerated carriers with enough long-lifetime to participate in the interface reactions [11–13], such as, Zhang and co-workers developed the redox cocatalysts modified strategy to solve the charge separation and migration problems of semiconductor and achieved considerable overall water splitting performance [14].

The water splitting was first reported in 1972 based on n-type $TiO_2$, whose light absorption is limited to the UV region [15–22]. To efficiently utilize the energy of solar spectrum reaching the Earth, numerous visible-light-responsive semiconductor candidates such as $WO_3$, CdS and $BiVO_4$ etc., have been reported [7,12,13,18–21]. However, most of them are only active in the half reaction (water reduction or oxidation). To date, semiconductors with considerable efficiency for direct water splitting still need to be developed.

Recently, Z-scheme water splitting system has been developed using two different semiconductors and a shuttle redox couple (Red/Ox) to achieve the overall water splitting [23–26]. The essen-

tial property of this system is similar to natural photosynthesis in green plants using the two separated PSII and PSI systems [27–29], which also contains two-step photo-induced oxidation and reduction reactions. The Redox pairs such as $IO_3^-/I^-$ and $Fe^{3+}/Fe^{2+}$ were usually employed to participate in the reactions with the photogenerated carriers of the two photocatalysts to close the cycles of $H_2$ and $O_2$ production [28]. To mimic nature-inspired Z-scheme, several artificial photocatalytic water-splitting systems have been developed with impressive solar energy-to-chemical efficiency. For example, Maeda et al. reported a new $BaZrO_3-BaTaO_2N$ solid solution with the absorption of visible photons up to 660 nm for the $H_2$ generation, and when coupled with rutile $TiO_2$, the Z-scheme obtained the 0.014% of solar energy conversion [25]. Tang et al. organized g-$C_3N_4$ and $WO_3$ or $BiVO_4$ to achieve the two-step Z-scheme pure water overall splitting under visible light irradiation [28]. For Z-scheme water splitting, one point should be pointed out, that is the reduction and oxidation processes should possess relatively high separation efficiency of photogenerated carriers. Li et al. constructed $MgTa_2O_{6-x}N_y/TaON$ heterostructure, which responded to the enhancement of $H_2$ evolution as one part of the Z-scheme, and acquired the apparent quantum efficiency (AQE) of 6.8% at 420 nm for overall water splitting when combined with $PtO_x/WO_3$ oxygen generation photocatalyst [30]. Nevertheless, there is still some room for the improvement of hydrogen generation through water overall splitting by designing new photocatalysts.

Material tight heterojunctions should have, in principle, the appropriate band positions of the two semiconductors for the energy level offsets, which create space charge accumulation/depletion at the interfaces of the two components for the final promotion of the dissociation of photogenerated carriers [30–32]. Polymeric g-$C_3N_4$ has been extensively reported as a robust metal-free semiconductor for solar energy conversion [33–36], especially hydrogen evolution [31,32,37–51], and several kinds of heterojunctions based on g-$C_3N_4$ have been developed with the considerable photocatalytic performance [31,46]. $TiO_2$ is another ideal hydrogen generation candidate [52–63], and the exposed facets of $TiO_2$ examples have been reported to greatly affect the photogenerated carrier's separation and migration efficiency [52]. On the other hand, it has been reported that layered g-$C_3N_4$ also owns the excellence of the 2D materials, which restricts and assists the specific morphology formation of the foreign species [41–43,52,53]. Constructing two skilled $H_2$-evolution photocatalysts to specific heterostructure for efficient photogenerated carrier's separation and solar-to-chemical energy conversion is still challenging. Herein, we will introduce an integrated design and synthesis of heterostructure with an emphasis on synergistic promotion on charge separation. The metal-free g-$C_3N_4$ and environment-friendly $TiO_2$ with (001) facet exposed are employed to fabricate the heterostructure as the $H_2$-evolution photocatalyst by one pot assembly and synthesis using bulk g-$C_3N_4$ and $TiCl_4$ as the precursors. When the heterojunction samples coupled with $O_2$-evolution photocatalyst i.e. $\beta$-Ni(OH)$_2$ modified $WO_3$ or $BiVO_4$, we successfully construct photocatalytic Z-scheme overall water splitting system with the apparent quantum efficiency of about 4% under visible light irradiation.

## 2. Experimental

### 2.1. Preparation of photocatalysts

All of the chemical reagents of analytical grade were purchased from Alfa Aesar Chemical Co. and used as received without further purification. And distilled water was used in all experiments.

Preparation of $TiO_2/C_3N_4$ heterojunction samples: 0.2 mol/L $TiCl_4$ transparent aqueous solution was first prepared as following

processes. $TiCl_4$ was slowly dropwise added into ice water under stirring [62]. 0.5 g bulk g-$C_3N_4$, synthesized via the thermal condensation of urea under the nitrogen atmosphere at 550 °C for 4 h, was added into the 5, 10, 15 and 20 mL 0.2 mol/L $TiCl_4$ aqueous solution, respectively. The 70 mL mixture was transferred into a 100 mL Teflon-lined autoclave for static crystallization at 150 °C for 24 h. The autoclave was naturally cooled to room temperature and the resulting powder was collected by centrifugation and washed with distilled water and ethanol three times. The obtained powder was dried at 80 °C for 12 h. The final products are denoted as $TiO_2/C_3N_4$-1, $TiO_2/C_3N_4$-2, $TiO_2/C_3N_4$-3 and $TiO_2/C_3N_4$-4, respectively, for further use.

Preparation of $WO_3$, $BiVO_4$ and corresponding loaded samples: $WO_3$ nanoparticles were synthesized through one-step simple hydrolysis process. 0.5 g $WCl_6$ was added into 30 mL distilled water and then heated this mixture to obtain the powder, which was finally calcinated at 500 °C. $BiVO_4$ was synthesized through the literature process [20]. $\beta$-Ni(OH)$_2$ or $PtO_x$ was loaded on $WO_3$ and $BiVO_4$ through the traditional impregnation method and the amount of loading was controlled ca. 1%. For the $\beta$-Ni(OH)$_2$ and $PtO_x$ co-loading on the oxygen generation photocatalysts, $\beta$-Ni(OH)$_2$ and $PtO_x$ were treated through the impregnation process successively.

### 2.2. Characterization techniques

The X-ray diffraction (XRD) patterns of studied samples were recorded on a Rigaku Smartlab-9 kW powder diffractometer using Cu K$\alpha$ X-ray ($\lambda$ = 1.54186 Å) tubes at a scanning rate of 4o/min in the region of 2$\theta$ = 10–80°.

Diffuse reflectance ultraviolet-visible (UV–vis) spectra of samples (ca. 20 mg diluted in ca. 80 mg $BaSO_4$) were recorded in air against $BaSO_4$ in the region of 200–800 nm on a PerkinElmer Lambda 950 spectrophotometer.

Transmission electron microscopy (TEM) images were taken on a FEI Tecnai G2 F20 electron microscope at an acceleration voltage of 200 kV. A few drops of alcohol suspension containing the sample were placed on a carbon-coated copper grid, followed by evaporation at ambient temperature.

X-ray photoelectron spectra (XPS) were recorded on a Kratos Axis Ultra DLD spectrometer with a monochromated Al-Ka X-ray source (hv = 1486.6 eV), hybrid (magnetic/electrostatic) optics and a multi-channel plate and delay line detector (DLD). All spectra were recorded by using an aperture slot of 300*700 μm, survey spectra were recorded with a pass energy of 160 eV and high-resolution spectra with a pass energy of 40 eV. Accurate binding energies ($\pm$0.1 eV) were determined with respect to the position of the adventitious C 1s peak at 284.8 eV.

Photoluminescence (PL) spectra were recorded on a Perkin Elmer LS55 fluorescence spectrophotometer. The samples of ca. 200 mg were dry-pressed into self-supporting wafers and then illuminated by an incident light of 320 nm at ambient temperature.

Fourier transform infrared reflectance (FTIR) spectra of samples were carried out on a Bruker EQUINX55 spectrometer with 128 scans at a resolution of 2 cm$^{-1}$. The spectra were recorded in dry air with KBr as the background.

Thermogravimetric (TG) analysis was carried out on a Q1000DSC + LNCS + FACS Q600SDT of TA Instruments under $N_2$ condition.

Atomic force microscopy (AFM) images were obtained by using a Bruker Multimode 8 in the tapping mode.

### 2.3. Photocurrent measurement

Electrochemical analysis was conducted in a conventional three-electrode cell on a Zennium Zahner electrochemical work-

station with the Ag/AgCl (saturated KCl) and Pt as the reference and counter electrode, respectively. The studied samples were ground roughly and then 5 mg was dispersed in 0.5 mL of DMF. The mixture was treated by sonication to obtain a slurry, which was spread onto FTO glass (**NOTE**: FTO glass should be treated through sonication in acetone, ethanol and deionized water, successively, and then nitrogen purging to ensure catalysts successful coating). For improving adhesion, the working electrode was further dried at 373 K for 2 h. 0.5 M $Na_2SO_4$ was used as the electrolyte for the photocurrent response measurement.

### 2.4. Water splitting reaction

Water photosplitting was performed in a home-made side-irradiation-type Pyrex reaction cell connected to a closed gas circulation and evacuation system under the irradiation of 150W Xe lamp (wavelength: from 200 to 2500 nm). In a typical experiment, catalyst sample of 200 mg was suspended in ca. 200 mL aqueous solution in the reaction cell, 0.01 M $AgNO_3$ for $O_2$ generation and 10% (v/v) triethanolamine-water solution for $H_2$ generation. After evacuation for 30 min, the reactor cell was irradiated at a constant temperature of 298 K under stirring. The gaseous products were analyzed by an on-line gas chromatograph (Shanghai GC122) with a thermal conductivity detector.

For the Z-scheme overall water splitting, 0.1 g hydrogen generation photocatalyst and 0.1 g oxygen evolution photocatalyst were added into 200 mL 5 mM NaI or 2 mM $FeCl_2$ aqueous solution.

### 2.5. Apparent quantum efficiency (AQE) measurement

The apparent quantum efficiency (AQE) was measured using the water splitting experimental setup. Five LED lamps with the wavelength of 280, 365, 405, 425 and 460 nm were chosen for the measurement. The AQE was calculated by the following equation:

$$AQE = (n \times \triangle G)/(I) \times 100\%$$
$$= (n \times 237)/(W \times S \times t) \times 100\%$$

n: the mole number of $H_2$ generation; $\triangle G$: 237 kJ/mol, that is the needed energy of one molecule water entirely splitting into $H_2$ and $O_2$; W: the power of LED lamp; S is the irradiated area and the t represents the reaction time.

## 3. Results and discussion

### 3.1. Synthesis and characterization of $TiO_2$/$C_3N_4$ heterojunction

Fig. 1 shows the XRD patterns of the obtained g-$C_3N_4$/$TiO_2$ heterojunction samples. Clearly, all the as-prepared samples give the typical layered g-$C_3N_4$ and anatase $TiO_2$ signals, without the appearance of trace impurity phase. For g-$C_3N_4$ signal, only one diffraction peak at ca. 27.4°, which reflects the information of interlayer stacking of aromatic systems can be found and meanwhile the peak at ca. 13.0° almost disappear for all samples. These results suggest that the bulk g-$C_3N_4$ has been exfoliated to thin-layer [61]. Besides, the relative intensity of g-$C_3N_4$ (002) peak at $2\theta = 27.4°$ decreases with increasing $TiO_2$ loading and almost disappear for the $TiO_2$/$C_3N_4$-4 sample. According to the $TiO_2$ diffraction peaks, anatase $TiO_2$ is demonstrated to be formed with the peaks at $2\theta = 25.3°$, 37.8°, 48°, 53.9°, 62.1° and 70.3° assigned to (101), (004), (200), (105), (213) and (220) lattice planes, and the intensities increase with the increasing amount of $TiO_2$. The $TiO_2$ particle size was calculated to be similar for all the samples based on Scherer equation calculation (Table S1). In contrast, pure phase of anatase $TiO_2$ cannot be formed if the preparative system is free of $C_3N_4$ (Fig. S1), demonstrating the interaction between $C_3N_4$ and anatase $TiO_2$.

Fig. S2 gives the corresponding TG results obtained under $N_2$ atmosphere of the studied samples. For g-$C_3N_4$, the TG curve gave
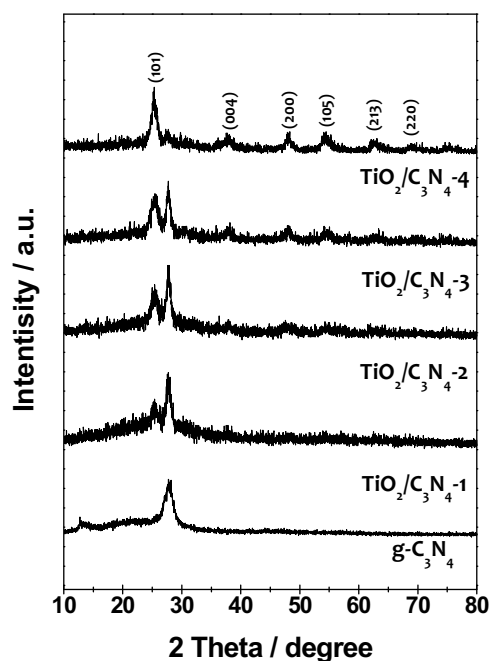


**Fig. 1.** XRD patterns of the synthesized $TiO_2$/$C_3N_4$ heterojunction samples under the specific conditions.

the complete weight loss at 720 °C. For the $TiO_2$/g-$C_3N_4$ heterojunctions, the TG results exhibited the different mass loss with pure g-$C_3N_4$, all the samples were found to show the weight loss at ca.580 °C, suggesting the heterojunction samples giving the lower thermal stability than g-$C_3N_4$. Our results are similar to previous works such as g-$C_3N_4$/$Bi_2MoO_6$ heterojunctions [33].

In Fig. S3, FTIR spectra of the studied samples is also given to exhibit the structure information. In the spectra of all $TiO_2$/g-$C_3N_4$ heterojunctions, the distinctive stretch modes do not give any obvious change with g-$C_3N_4$, and the structural integrity of g-$C_3N_4$ is directly proved. Specially, the broad absorption bands at 1200–1650 cm$^{-1}$ are assigned to either C=N or C-N stretching vibrations [49–51] and the broad centered at 3120 cm$^{-1}$ is belong to the N—H stretching vibration. The characteristic absorption band at ca. 1615 and 3330 cm$^{-1}$, which are associated with the $TiO_2$ surface chemisorbed water molecular bond stretch [50,51]. No obvious $TiO_2$ FTIR features can be detected in the $TiO_2$/g-$C_3N_4$ samples, suggesting the limitation of $TiO_2$ surface water molecular.

The morphologies of as-synthesized $TiO_2$/$C_3N_4$ samples with different mass ratios are investigated by TEM, and the represented TEM images are shown in Fig. 2. Clearly, all of the as-prepared $TiO_2$/$C_3N_4$ samples appear as typical 2D nanosheets with nanoparticles loading image. More specifically, the particle size of loaded $TiO_2$ is ca. 10 nm for all samples, which is consistent with the XRD result. The $TiO_2$ displayed homogeneous dispersion on the thin-layered g-$C_3N_4$, as shown in Fig. 2(a)-(d) and Fig. S4. As seen in the high-resolution TEM (HRTEM) images, the well-ordered lattice fringes with interplanar spacing of 0.19 nm assigned to (001) facet of $TiO_2$ can be observed, indicating the high degree of crystallinity of loaded $TiO_2$ and the exposed (001) facet obtained. Fig. S5 shows the anatase $TiO_2$ mode from the z and a-axis directions. Also, the $TiO_2$ nanoparticles tightly attach to g-$C_3N_4$ from the HRTEM, and the strong interaction has been proved to be helpful for interface migration of the carriers, which is beneficial to the enhanced photocatalytic efficiency on the heterojunction system [31,60]. On the other hand, we also studied the morphologies of the reference samples as shown in Fig. S6. Nanoparticles and nanorods can be observed due to the $TiO_2$ mixture phase formation, confirming the
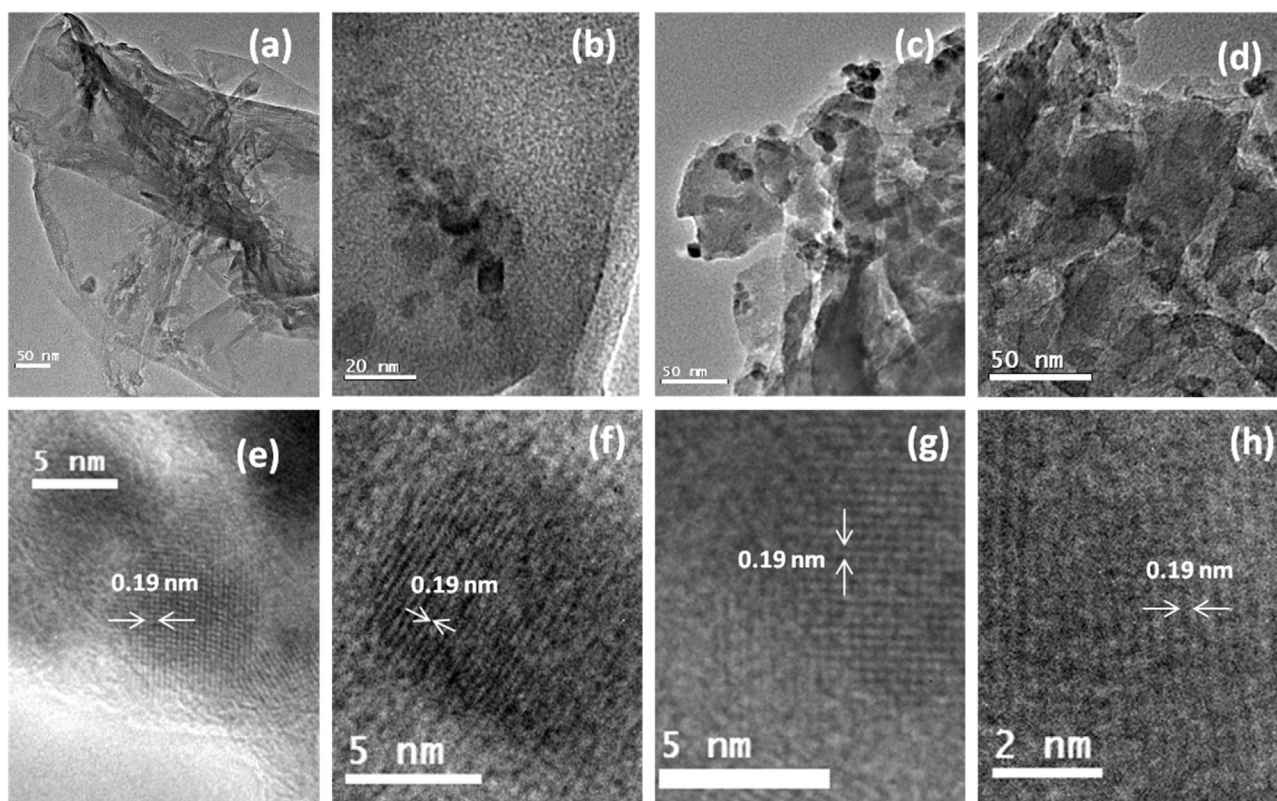
**Fig. 2.** TEM images of synthesized $TiO_2/C_3N_4$ heterojunction samples: (a)-(d) are the $TiO_2/C_3N_4$-1, $TiO_2/C_3N_4$-2, $TiO_2/C_3N_4$-3 and $TiO_2/C_3N_4$-4; (e)-(h) show the corresponding HRTEM results, $TiO_2/C_3N_4$-1, $TiO_2/C_3N_4$-2, $TiO_2/C_3N_4$-3 and $TiO_2/C_3N_4$-4.

template effect of layered $g$-$C_3N_4$. The element mapping was also carried out based on $TiO_2/C_3N_4$-3 sample and the results were given in Fig. S7, which further suggested the homogeneous deposition of $TiO_2$ nanoparticles on $C_3N_4$ surface. Fig. S8 gives the AFM results of the studied heterojunction samples with the $g$-$C_3N_4$ thickness of ca.4.5 nm, suggesting the studied g-C3N4 consists of only about 13 atomic carbon nitride layers and further confirms the hydrothermal exfoliation process.

To study the surface and sub-surface chemical states (in the depth up to 5 nm) of $TiO_2/C_3N_4$ heterojunction samples, X-ray photoelectron spectroscopy (XPS) analysis was performed and the results were shown in Fig. 3. In C 1s region, binding energy values centered at around 288.4 and 284.9 eV are observed for both g-$C_3N_4$ and $TiO_2/C_3N_4$ samples. The main contribution peak located at 288.4 eV is typically attributed to the $sp^2$-bonded carbon of N—C=N backbone in the aromatic ring of the g-$C_3N_4$ [48–51]; while the peak at 284.9 eV can be assigned to graphitic carbon or carbon contamination and also the $sp^2$-hybridized of C—N [33]. In this work, the relative intensity of peak located at 284.9 eV for the $TiO_2/C_3N_4$ samples is higher than pure g-$C_3N_4$ and shows an increasing trend with increasing $TiO_2$ loading. Therefore, we suggest the 284.9 eV peak may be originated from $CO_x$, which act as the adsorption sites for oxide heterogeneous nucleation [33]. The N 1s spectra in Fig. 3(b) can be deconvoluted into obvious three peaks centering at 398.7, 399.7 and 401.1 eV. The main peak at 398.7 eV is a typical signal for sp2-hybridized nitrogen (C—N=C) of triazine rings [33], and the peak centered at 399.7 eV is assigned to N—$(C)_3$ groups of the skeleton [33]. The last weak peak with the binding energy of 401.1 eV is attributed to the surface uncondensed bridging N atom with C—N—H functional groups attached [48–50]. In the Ti 2p region, two binding energy values located at 458.4 and 464.2 eV assignable to the typical $2p_{3/2}$ and $2p_{1/2}$ of $Ti^{4+}$ in $TiO_2$ [22,62] are observed for $TiO_2/C_3N_4$ samples. Moreover and interestingly, the

main peak at 458.4 eV shifts toward the higher binding energy from the modified Ti 2p region as showed in Fig. S9, and these results directly suggest the heterogeneous growth of $TiO_2$ on g-$C_3N_4$ [62].

On the basis of above information on the synthesized $TiO_2/C_3N_4$ heterojunctions, the formation process can be illustrated in Fig. 4. $TiCl_4$ was used as the $TiO_2$ precursor and would react with water to form the $Ti(OH)_x^-$ and HCl [22,62]. The formed $TiO_2$ precursor inserted into the interval of layered g-$C_3N_4$ and adsorbed onto the active group sites. Then under the high temperature hydrothermal condition and through the heterogeneous nucleation process, the $Ti(OH)_x^-$ changed into the $TiO_2$ and the bulk g-$C_3N_4$ turn into thin layers. For obtaining of the exposed (001) facets anatase $TiO_2$, fluorinion is serviceable owing to its strong adsorptivity and reduction of the surface energy [59]. In our present work, interestingly, we found that the layered g-$C_3N_4$ could guide the $TiO_2$ (001) facets exposing with pure anatase phase (Fig. 2 and Figs. S4–S6). This can be explained by the restriction effect of two dimension (2D) layered structure [52].

The optical absorption properties of studied samples were investigated by diffuse reflectance UV–vis spectroscopy. As shown in Fig. S10, all samples show similar absorption up to 410 nm of visible-light region attributed to the band-band transition of g-$C_3N_4$. The absorption edges are almost the same as each other with the threshold value of 450 nm and no obvious red or blue shift can be detected, which suggest the introduction of $TiO_2$ nanoparticles do not change the intrinsic absorption of g-$C_3N_4$. Moreover, a decrease trend in the light absorption with increasing of $TiO_2$ loading can be observed, which can be explained from the enhanced incident light scattering owing to $TiO_2$ absorption effect.

The room-temperature photoluminescence (PL) spectrum, which comes from the released recombination energy of photo-generated carriers [60,62], was carried out and the corresponding results were given in Fig. S11. Noticeably, the PL intensity of
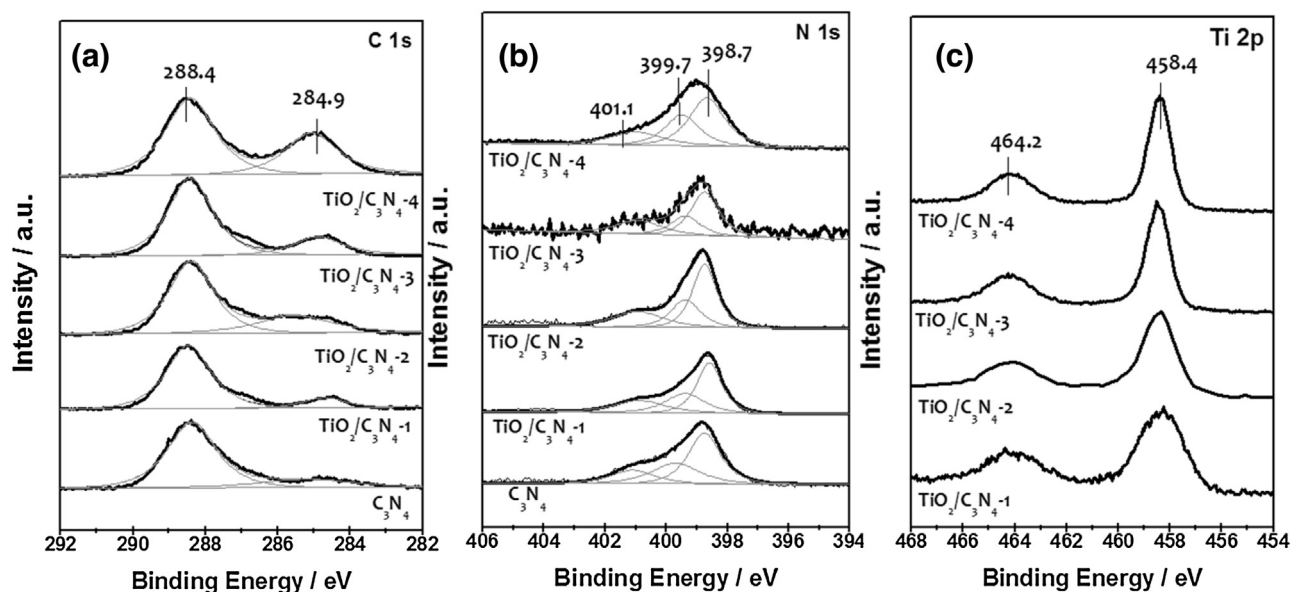
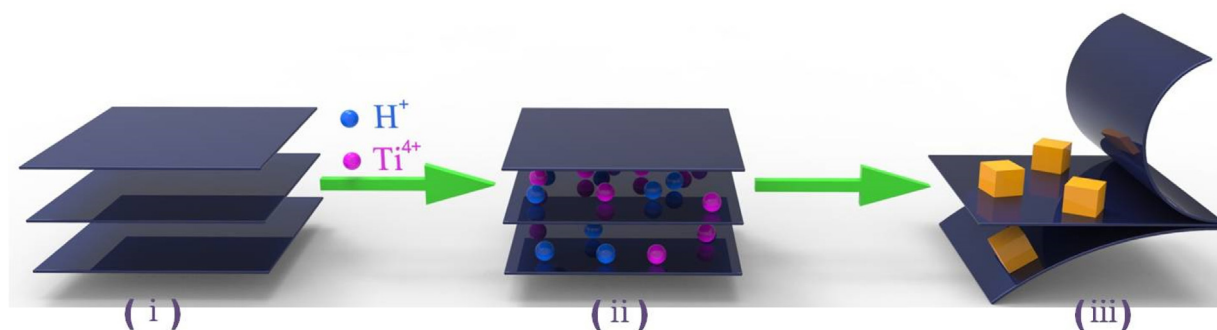**Fig. 3.** XPS spectra of heterojunction samples, (a) C 1s, (b) N 1s and (c) Ti 2p.



**Fig. 4.** Schematic illustration of the bulk g-$C_3N_4$ induced anatase $TiO_2$ formation with (001) facets exposed and for the construction of heterojunction structure. (i)-(ii) $Ti^{4+}$ ions combine with $H_2O$ molecules to form $Ti(OH)_x^-$ and insert into the layered g-$C_3N_4$ framework, and then adsorb onto the reaction sites; (ii)-(iii) the adsorbed $Ti(OH)_x^-$ ions heterogeneous nucleation between the g-$C_3N_4$ layers under the restriction and template effect of layers, and finally the pure anatase $TiO_2$ with exposed (001) facet is in situ formed with bulk g-$C_3N_4$ turn into thin layers through the self-exfoliation effect.

$TiO_2/C_3N_4$ samples is lower than pure g-$C_3N_4$, and the PL intensity can be linked together with the number of carriers participating in the recombination [60]. Therefore, the PL results suggest the good separation ability of carriers in the as-synthesized materials compared to bare g-$C_3N_4$. Interestingly, the PL intensity is not always decreasing with the increase of $TiO_2$ loading, and $TiO_2/C_3N_4$-3 shows the lowest PL intensity, revealing that a certain number of heterojunctions sites can promote the separation of photogenerated carriers [60].

### 3.2. Hydrogen generation based on $TiO_2/C_3N_4$ heterojunction

The photocatalytic $H_2$ evolution rates on the obtained $TiO_2/C_3N_4$ samples were first examined in the presence of triethanolamine. As seen in Fig. 5(a), compared to the pristine g-$C_3N_4$, the photocatalytic $H_2$ evolution rate on the heterostructures increased to a different extent, e.g. from ca. 49 to 154 umol h$^{-1}$. The enhanced hydrogen generation performance of $TiO_2/C_3N_4$ samples suggests not only the superiority of two-component composite system for the carrier separation, but also the synergistic effect of one more participants. It should be noted that the trend of solar-to-hydrogen is well in accordance with the PL results. To obtain the stability information of $TiO_2/C_3N_4$ samples, the recycling experiment of hydrogen generation rate based on $TiO_2/C_3N_4$-3 was carried out. As

shown in Fig. 5(b), no obvious hydrogen generation rate decreases can be detected within five cycles in 20 h, directly showing the photo-stabilization of as-synthesized heterojunction structure. The XRD, TEM and XPS results of the studied $TiO_2/C_3N_4$-3 sample after the cycle hydrogen evolution as shown in Fig. S12 and S13, which further confirm the above stability result. On the other hand, photocurrent response was also carried out to obtain more information about separation efficiency of photogenerated carriers, which was relative to reduction of proton by electrons. Fig. 6(a) shows the respective experimental results. Under irradiation, the photocatalysts showed obvious photocurrent response under the scan rate of 50 mV s$^{-1}$ from negative to positive potential. Also, the photocurrent value increases with increasing $TiO_2$ loading, indicating more heterojunction formation for free carriers generation. Please note that the here photocurrent measurements maybe result from the $TiO_2$ nanoparticles adhering to the FTO glass.

Fig. 6(b) shows the band alignment between the two materials, $TiO_2$ and g-$C_3N_4$, which suggests the typical Type II heterojunction structure [31,32]. The conductive band offset between the two samples can drive the transformation of photogenerated electrons from g-$C_3N_4$ to $TiO_2$. And this effect not only can inhibit the recombination of photogenerated carriers, but also increase the reduction sites of $H^+$ to $H_2$, then responses to the enhanced $H_2$ generation and photocurrent value.
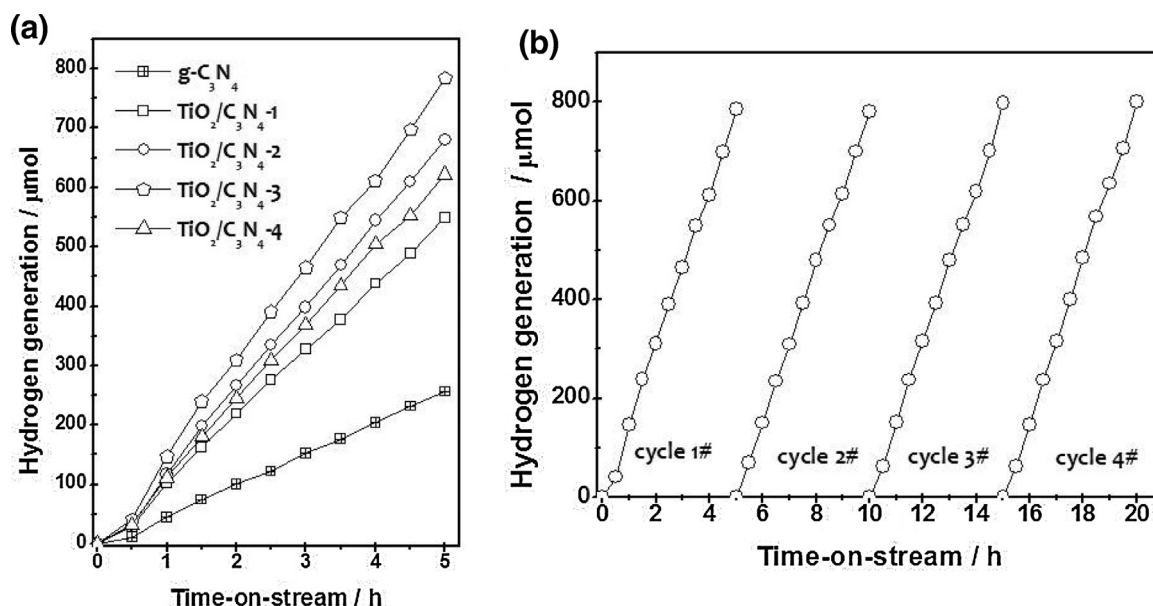
**Fig. 5.** (a) Hydrogen generation rate from water photo-splitting under layered g-C$_3$N$_4$ and series of synthesized TiO$_2$/C$_3$N$_4$ samples; (b) the cycled hydrogen evolution performance under the TiO$_2$/C$_3$N$_4$-3 sample. Reaction conditions: 0.1 g catalyst, 200 mL 10% (v/v) triethanolamine-water solution, 1% Pt was in situ loaded as the co-catalyst, 150W Xenon lamp without filters used as the light source.
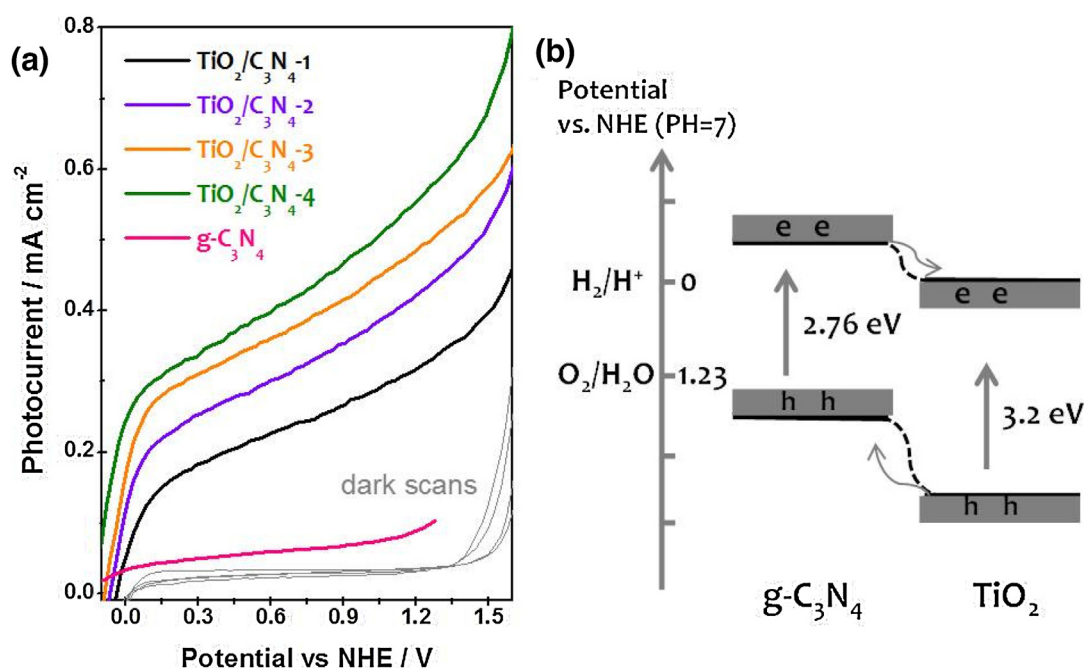


**Fig. 6.** (a) Photocurrent response of samples in 0.5 M Na$_2$SO$_4$ solution with the scan rate of 50 mV s$^{-1}$ from negative to positive potential; (b) schematic illustration of heterojunction formed between g-C$_3$N$_4$ and TiO$_2$.

### 3.3. Z-scheme overall water splitting performance of TiO$_2$/C$_3$N$_4$ heterojunction

Z-scheme overall water splitting involves two types of semiconductors, which participate in the reduction and oxidation reaction of water splitting through two separate steps [23,24]. And a soluble redox mediator such as I$^-$/IO$_3$$^-$ or Fe$^{2+}$/Fe$^{3+}$ is essential to complete the electron transfer between the two photocatalysts favorably [26]. More specifically, the two steps can be explained as follows. A low valence state and easily oxidized ions (such as I$^-$ or Fe$^{2+}$) are used as the precursor of shuttle redox mediator, at the first step, one photocatalyst takes part in the half reaction of water

splitting i.e. the reduction of proton to H$_2$ and oxidizes the ions to high valence state (such as IO$_3$$^-$ or Fe$^{3+}$), the concentration of generated oxidation ions reaches a certain level and then triggers the other photocatalyst participating in the other half reaction of water splitting, that is oxygen generation step [28,64]. According to above procedure of the Z-scheme system, the hydrogen generation photocatalyst should own ideal separation ability of charge and enough oxidative level for the redox mediator's formation and then ensure next half reaction going on well.

For the synthesized TiO$_2$/C$_3$N$_4$ heterojunction samples, the high photogenerated charge separation efficiency and considerable hydrogen generation have been confirmed. And to achieve good

**Table 1**

The overall water splitting performance based on $H_2$ generation photocatalyst of $TiO_2/C_3N_4$ samples and oxygen photocatalysts of $WO_3$ or $BiVO_4$. 150 W xenon lamp without filters used as the light source, and the amount of catalysts was controlled to *ca.* 0.1 g.

| Entry | $H_2$ photocatalyst[a] | $O_2$ photocatalyst | Redox mediator | Gas generation rate ($\mu mol\,h^{-1}$) | |
|---|---|---|---|---|---|
| | | | | $H_2$ | $O_2$ |
| 1 | $TiO_2$[b] | $WO_3$ (1%$PtO_x$) | NaI (5 mM) | – | – |
| 2 | g-$C_3N_4$ | $WO_3$ (1%$PtO_x$) | NaI (5 mM) | 0.7 | 0.3 |
| 3 | $TiO_2/C_3N_4$-1 | $WO_3$ (1%$PtO_x$) | NaI (5 mM) | 8.53 | 4.32 |
| 4 | $TiO_2/C_3N_4$-2 | $WO_3$ (1%$PtO_x$) | NaI (5 mM) | 9.35 | 4.68 |
| 5 | $TiO_2/C_3N_4$-3 | $WO_3$ (1%$PtO_x$) | NaI (5 mM) | 10.23 | 5.28 |
| 6 | $TiO_2/C_3N_4$-4 | $WO_3$ (1%$PtO_x$) | NaI (5 mM) | 8.96 | 4.46 |
| 7 | $TiO_2/C_3N_4$-3 | $BiVO_4$ (1%$PtO_x$) | NaI (5 mM) | 6.3 | 3.12 |
| 8 | $TiO_2/C_3N_4$-3 | $WO_3$ (1%$PtO_x$) | $FeCl_2$ (2 mM) | 5.88 | 2.86 |
| 9 | $TiO_2/C_3N_4$-3 | $WO_3$ (1.5%$PtO_x$) | NaI (5 mM) | 9.43 | 4.62 |
| 10 | $TiO_2/C_3N_4$-3 | $WO_3$ (0.5%$PtO_x$) | NaI (5 mM) | 9.02 | 4.43 |
| 11 | $TiO_2/C_3N_4$-3 | $\beta$-$Ni(OH)_2/WO_3$ | NaI (5 mM) | 9.7 | 5.1 |
| 12 | $TiO_2/C_3N_4$-3 | $\beta$-$Ni(OH)_2/WO_3$($PtO_x$) | NaI (5 mM) | 50.2 | 24.3 |
| 13 | $TiO_2$ | $\beta$-$Ni(OH)_2/WO_3$($PtO_x$) | NaI (5 mM) | 0.5 | 0.23 |
| 14 | $C_3N_4$ | $\beta$-$Ni(OH)_2/WO_3$($PtO_x$) | NaI (5 mM) | 6.45 | 3.33 |
| 15[c] | g-$C_3N_4$(3%$PtO_x$) | $WO_3$(0.5%$PtO_x$) | NaI (5 mM) | 7.4 | 3.7 |

[a] 1%Pt was photo-deposited on the $H_2$ photocatalyst as the co-catalyst.
[b] Anatase $TiO_2$ was synthesized through our previous work [62].
[c] The value was obtained from the literature [28].

Z-scheme overall water splitting, the samples should own the relative oxidation ability as discussed above. Then, the half reaction i.e. oxygen evolution of water splitting was measured using $AgNO_3$ as the electron scavenger and Fig. S14 showed the corresponding results. Clearly, the compounds show the enhanced oxygen generation compared to bare g-$C_3N_4$, and these results further confirm the good carrier separation ability. It should be mentioned that the oxidation of $I^-$ to $IO_3^-$ is favorable in comparison to water oxidation, so the usage of $I^-$ as the hole scavenger should induce the water reduced to $H_2$. Next, we chose the $TiO_2/C_3N_4$-3 sample for the further experimentation. For pure water, only a small quantity of $H_2$ and $O_2$ gas chromatography (GC) signals were detected after 10 h in our experiment system, which suggested the infeasibility for obtaining considerably water splitting efficiency based on single catalyst system. For the further Z-scheme experiment carrying out, we first confirmed the attempt of $I^-$ as hole scavenger based on $TiO_2/C_3N_4$-3 sample, Fig. S15 shows the corresponding results. Hydrogen generation was observed and these results indicated that the $I^-$ anions could act as effective electron donors for the water splitting. Based on the above attempts, Z-scheme water overall splitting could be carried out by coupling with $O_2$ evolution photocatalysts.

Table 1 gives the photocatalytic Z-scheme water splitting performance using typical samples and redox mediators. In most of cases, the molar ratio of $H_2$ and $O_2$ evolved is close to 2:1, indicating the feasibility of overall water splitting. The photocatalytic Z-scheme overall water splitting performances are not only strongly dependent on the $H_2$-evolution photocatalysts used, but also greatly affected by the $O_2$-evolved side as well as redox mediators. Compared to the pristine $TiO_2$ or g-$C_3N_4$ (entries 1 and 2), the photocatalytic Z-scheme overall water splitting performances using $TiO_2/C_3N_4$-n heterostructure as $H_2$-evolution photocatalyst (entries 3–6) are all remarkably enhanced. Using the optimum $TiO_2/C_3N_4$-3 sample as $H_2$-evolution photocatalyst, we further examined the effect of $O_2$-evolution photocatalyst. It is found that $WO_3$ exhibits the optimal value as seen in entry 6. The other redox mediator $Fe^{2+}$ was also tested as the redox mediator for the Z-scheme water overall splitting into $H_2$ and $O_2$ and presents the relative weak acceleration of water splitting (entry 8). To obtained further enhanced performance, we focused on the two photocatalysts of $TiO_2/C_3N_4$-3 and $WO_3$ to regulate the used amount of co-catalysts of oxygen generation photocatalyst as summarized in entries 9 and 10. Clearly, 1% $PtO_x$ loading seems to be the optimum content. Interestingly, when $\beta$-$Ni(OH)_2$ was used for replacing the

**Table 2**

Overall water splitting performance and corresponding AQE values under different LEDs monochromatic light irradiation.

| LED wavelength/nm | Power/mW/cm$^2$ | Gas evolution/$\mu mol$ | | AQE/% |
|---|---|---|---|---|
| | | $H_2$ | $O_2$ | |
| 365 | 8.3 | 45.6 | 22.3 | 4.94 |
| 405 | 8.6 | 38.36 | 18.47 | 4.01 |
| 425 | 5.4 | 12.39 | 7.02 | 2.06 |
| 460 | 6.3 | – | – | – |

Reaction conditions: catalysts: $TiO_2/C_3N_4$ (1%Pt) and $\beta$-$Ni(OH)_2/WO_3$($PtO_x$), 0.1 g; 200 mL 5 mM NaI aqueous solution; reaction time: 1 h.

noble $PtO_x$ with the same amount under the $I^-/IO_3^-$ redox mediator, the water splitting efficiency reached almost the same value (entry 11). $\beta$-$Ni(OH)_2$ may be propitious to the photogenerated holes transfer, that is responses to the separation of carriers and then the considerable gas evolution. We also loaded 1% $PtO_x$ on the surface of $\beta$-$Ni(OH)_2/WO_3$ and the water overall splitting gave the further enhanced performance with the $H_2$ and $O_2$ generation of 50.2 and 24.3 $\mu mol\,h^{-1}$, respectively, as listed in entry 12. And the value is ca. 5 times higher than the $WO_3$($PtO_x$) (entry 5), suggesting the co-work of two components of $\beta$-$Ni(OH)_2$ and $PtO_x$ for the separation of photogenerated carriers and the promoting of oxygen evolution. To our best knowledge, there is no report about the usage of two oxygen-evolution co-catalysts for the final synergistic effect with the best application. On the other hand, the Z-scheme overall water splitting based on g-$C_3N_4$ material was also listed in Table 1 to compared with our discussional heterogeneous samples (entry 15). Notably, the superiority of our synthesized $TiO_2/C_3N_4$ samples in promotion the separation of photogenerated carriers was demonstrated.

To give the widely accepted comparison of water splitting ability, the apparent quantum efficiency (AQE) measurement was carried out under different illumination as summarized in Table 2. Thinking above results, $TiO_2/C_3N_4$-3 and $WO_3$ were chosen as the hydrogen and oxygen evolution photocatalysts, and 0.5 mM NaI was the corresponding aqueous solution. As given in Table 2, five monochromatic LED lights with the corresponding power (mW/cm$^2$) were also listed. Under the specially designated conditions, all the producible $H_2$ and $O_2$ evolution values from pure water show the theoretical molar ratio with ca. 2:1. It should be pointed out that the comparative experiment of $WO_3$($PtO_x$) and $\beta$-$Ni(OH)_2/WO_3$($PtO_x$) show the obvious difference under the two chosen wavelengths of 365 and 405 nm. That is, under the $\beta$-

Ni(OH)$_2$/WO$_3$(PtO$_x$) condition, the AQE values are almost 4 times higher than the comparable WO$_3$(PtO$_x$) condition, which corresponds to above results and further suggests the importance of introducing β-Ni(OH)$_2$ for the Z-scheme cycle carrying on. More specifically, the AQE values are 4.94% and 4.01% under the 365 and 405 nm, respectively. And under the irradiation of 425 nm monochromatic light, the AQE is 2.06%, which is higher than our previous value of half reaction (H$_2$ generation) [22].

## 4. Conclusions

In conclusion, we developed a one-step hydrothermal process to synthesize TiO$_2$/C$_3$N$_4$ heterojunction structure using bulk g-C$_3$N$_4$ and titanium tetrachloride as the precursors. The layered g-C$_3$N$_4$ structure provided the heterogeneous nucleation template for sub-10 nm pure anatase TiO$_2$ nanoparticles with (001) facet exposed. Meanwhile, with the growth of TiO$_2$, the bulk g-C$_3$N$_4$ turned into thinner nanosheets through the self-exfoliation process. Characterization results from XRD and TEM indicate the existence of TiO$_2$ nanoparticles and g-C$_3$N$_4$ nanosheets. Further results from XPS spectra provides information on the strong interaction between TiO$_2$ and g-C$_3$N$_4$, which is beneficial to the interface transfer of photogenerated carriers.

The assembled TiO$_2$/C$_3$N$_4$ samples are active in the hydrogen evolution half reaction of water splitting with the best performance of 154 μmol h$^{-1}$ and good photo-stability. When combining with WO$_3$ or BiVO$_4$ oxygen generation photocatalysts, the Z-scheme overall water splitting under the I$^-$/IO$_3^-$ or Fe$^{2+}$/Fe$^{3+}$ redox mediator conditions, the H$_2$ and O$_2$ production with a mole ratio of 2 could be realized. With the loading of β-Ni(OH)$_2$ on the WO$_3$ and BiVO$_4$, an almost 6 times enhancement in Z-scheme cycle performance was obtained. The AQE values of studied Z-scheme pure water splitting under 365 and 405 nm are 4.94% and 4.01% under optimized conditions. The one-pot hydrothermal method based on bulk g-C$_3$N$_4$ will shed a light on the design of new heterojunctions for Z-scheme overall water splitting.

## Acknowledgements

## Appendix A. Supplementary data

Supplementary data associated with this article can be found, in the online version, at http://dx.doi.org/10.1016/j.apcatb.2016.03.026.

## References

[1] Y. Ma, X. Wang, Y. Jia, X. Chen, H. Han, C. Li, Chem. Rev. 114 (2014) 9987–10043.
[2] J. Barber, Chem. Soc. Rev. 38 (2009) 185–196.
[3] Y. Tachibana, L. Vayssieres, J.R. Durrant, Nature Photon. 8 (2012) 511–518.
[4] S.L. Nathan, G.N. Daniel, PNAS 103 (2006) 15729–15735.
[5] S.J.A. Moniz, S.A. Shevlin, D.J. Martin, Z.-X. Guo, J. Tang, Energy Environ. Sci. 8 (2015) 731–759.
[6] S.S.K. Ma, T. Hisatomi, K. Maeda, Y. Moriya, K. Domen, J. Am. Chem. Soc. 134 (2012) 19993–19996.
[7] K. Maeda, K. Domen, J. Phys. Chem. C 111 (2007) 7851–7861.
[8] J. Sato, N. Saito, Y. Yamada, K. Maeda, T. Takata, J.N. Kondo, M. Hara, H. Kobayashi, K. Domen, Y. Inoue, J. Am. Chem. Soc. 127 (2005) 4150–4151.
[9] K. Maeda, K. Teramura, D. Lu, T. Takata, N. Saito, Y. Inoue, K. Domen, Nature 440 (2006) 295.
[10] X.C. Wang, K. Maeda, A. Thomas, K. Takanabe, G. Xin, J.M. Carlsson, K. Domen, M. Antonietti, Nat. Mater. 8 (2009) 76–80.
[11] Z. Zou, J. Ye, K. Sayama, H. Arakawa, Nature 414 (2001) 625–627.
[12] T. Takata, A. Tanaka, M. Hara, J.N. Kondo, K. Domen, Catal. Today 44 (1998) 17–26.
[13] K. Maeda, K. Domen, J. Phys. Chem. Lett. 1 (2010) 2655–2661.
[14] G. Zhang, Z.-A. Lan, L. Lin, S. Lin, X. Wang, Chem. Sci. (2016), http://dx.doi.org/10.1039/C5SC04572J.
[15] A. Fujishima, K. Honda, Nature 238 (1972) 37–38.
[16] S.U.M. Khan, M. Al-Shahry, W.B. Ingler Jr., Science 297 (2002) 2243–2245.
[17] X. Chen, L. Liu, P.Y. Yu, S.S. Mao, Science 331 (2011) 746–750.
[18] G. Hodes, D. Cahen, J. Manassen, Nature 260 (1976) 312–313.
[19] K. Sayama, A. Nomura, Z. Zou, R. Abe, Y. Abe, H. Arakawa, Chem. Commun. 23 (2003) 2908–2909.
[20] R. Li, F. Zhang, D. Wang, J. Yang, M. Li, J. Zhu, X. Zhou, H. Han, C. Li, Nat. Commun. 4 (2013) 1432.
[21] Y. Hu, X. Gao, L. Yu, Y. Wang, J. Ning, S. Xu, X.W. Lou, Angew. Chem. Int. Ed. 126 (2014) 6027–6031.
[22] L. Li, J. Yan, T. Wang, Z.J. Zhao, J. Zhang, J. Gong, N. Guan, Nat. Commun. 6 (2015) 5881.
[23] K. Maeda, ACS Catal. 3 (2013) 1486–1503.
[24] R. Abe, J. Photochem. Photobiol. C 11 (2010) 179–209.
[25] K. Maeda, D. Lu, K. Domen, ACS Catal. 3 (2013) 1026–1033.
[26] M. Bowker, Green Chem. 13 (2011) 2235–2246.
[27] K.N. Ferreira, T.M. Iverson, K. Maghlaoui, J. Barber, S. Iwata, Science 303 (2004) 1831–1838.
[28] D.J. Martin, P.J.T. Reardon, S.J.A. Moniz, J. Tang, J. Am. Chem. Soc. 136 (2014) 12568–12571.
[29] K. Maeda, M. Higashi, D. Lu, R. Abe, K. Domen, J. Am. Chem. Soc. 132 (2010) 5858–5868.
[30] S. Chen, Y. Qi, T. Hisatomi, Q. Ding, T. Asai, Z. Li, S.S.K. Ma, F. Zhang, K. Domen, C. Li, Angew. Chem. Int. Ed. 54 (2015) 8498–8501.
[31] J. Zhang, M. Zhang, R.-Q. Sun, X. Wang, Angew. Chem. Int. Ed. 124 (2012) 10292–10296.
[32] J. Tersoff, Phys. Rev. B 30 (1984) 4874.
[33] H. Li, J. Liu, W. Hou, N. Du, R. Zhang, X. Tao, Appl. Catal. B: Environ. 160–161 (2014) 89–97.
[34] G. Li, X. Nie, J. Chen, Q. Jiang, T. An, P.K. Wong, H. Zhang, H. Zhao, H. Yamashita, Water Res. 86 (2015) 17–24.
[35] K. Wang, Q. Li, B. Liu, B. Cheng, W. Ho, J. Yu, Appl. Catal. B: Environ. 176–177 (2015) 44–52.
[36] J. Xiao, J. Xiea, F. Nawaz, S. Jin, F. Duan, M. Li, H. Cao, Appl. Catal. B: Environ. 181 (2016) 420–428.
[37] Q. Han, B. Wang, Y. Zhao, C. Hu, L. Qu, Angew. Chem. Int. Ed. 54 (2015) 11433–11437.
[38] D.J. Martin, K. Qiu, S.A. Shevlin, A.D. Handoko, X. Chen, Z. Guo, J. Tang, Angew. Chem. Int. Ed. 53 (2014) 9240–9245.
[39] Y. Cui, J. Zhang, G. Zhang, J. Huang, P. Liu, M. Antonietti, X. Wang, J. Mater. Chem. 21 (2011) 13032–13039.
[40] Z. Chen, P. Sun, B. Fan, Z. Zhang, X. Fang, J. Phys. Chem. C 118 (2014) 7801–7807.
[41] J. Hong, Y. Wang, W. Zhang, R. Xu, ChemSusChem 6 (2013) 2263–2268.
[42] Y. Hou, A.B. Laursen, J. Zhang, G. Zhang, Y. Zhu, X. Wang, S. Dahl, I. Chorkendorff, Angew. Chem. Int. Ed. 52 (2013) 3621–3625.
[43] S. Cao, J. Low, J. Yu, M. Jaroniec, Adv. Mater. 27 (2015) 2150–2176.
[44] D. Zheng, C. Huang, X. Wang, Nanoscale 7 (2015) 465–470.
[45] Y. Zheng, L. Lin, B. Wang, X. Wang, Angew. Chem. Int. Ed. 54 (2015) 12868–12884.
[46] D. Zheng, G. Zhang, X. Wang, Appl. Catal. B: Environ. 179 (2015) 479–488.
[47] M.J. Muñoz-Batista, M.A. Nasalevich, T.J. Savenijec, F. Kapteijnb, J. Gascon, A. Kubacka, M. Fernández-García, Appl. Catal. B: Environ. 176–177 (2015) 687–698.
[48] D. Zheng, C. Pang, Y. Liu, X. Wang, Chem. Commun. 51 (2015) 9706–9709.
[49] D. Zheng, C. Pang, X. Wang, Chem. Commun. 51 (2015) 17467–17470.
[50] J. Zhang, Y. Chen, X. Wang, Energy Environ. Sci. 8 (2015) 3092–3108.
[51] D. Zheng, C. Huang, X. Wang, Nanoscale 7 (2015) 465–470.
[52] J. Xie, X. Sun, N. Zhang, K. Xu, M. Zhou, Y. Xie, Nano Energy 2 (2013) 65–74.
[53] K. Dai, L. Lu, C. Liang, Q. Liu, G. Zhu, Appl. Catal. B: Environ 156 (2014) 331–340.
[54] K. Dai, L. Lu, Q. Liu, G. Zhu, X. Wei, J. Bai, L. Xuan, H. Wang, Dalton Trans. 43 (2014) 6295–6299.
[55] Y. Hou, Z. Wen, S. Cui, X. Guo, J. Chen, Adv. Mater. 25 (2013) 6291–6297.
[56] K. Maeda, K. Teramura, K. Domen, J. Catal. 254 (2008) 198–204.
[57] J. Yan, G. Wu, W. Dai, N. Guan, L. Li, ACS Sustainable Chem. Eng. 2 (2014) 1940–1946.
[58] T. Tachikawa, S. Yamashita, T. Majima, J. Am. Chem. Soc. 133 (2011) 7197–7204.
[59] J. Pan, G. Liu, G.Q. Lu, H.M. Cheng, Angew. Chem. Int. Ed. 50 (2011) 2133–2137.
[60] J. Yan, G. Wu, N. Guan, L. Li, Appl. Catal. B: Environ. 152 (2014) 280–288.
[61] J. Zhang, M. Grzelczak, Y. Hou, K. Maeda, K. Domen, X. Fu, M. Antonietti, X. Wang, Chem. Sci. 3 (2012) 443–446.
[62] J. Yan, G. Wu, N. Guan, L. Li, Z. Li, X. Cao, Phys. Chem. Chem. Phys. 15 (2013) 10978–10988.
[63] J. Yan, Y. Zhang, S. Liu, G. Wu, L. Li, N. Guan, J. Mater. Chem. A 3 (2015) 21434–21438.
[64] R. Abe, T. Takata, H. Sugihar, K. Domen, Chem. Commun. 30 (2005) 3829–3831.